Journal of Environmental Chemical Engineering 10 (2022) 107107

Contents lists available at ScienceDirect

Journal of Environmental Chemical Engineering

journal homepage: www.elsevier.com/locate/jece

Enhanced selective adsorption and photocatalytic of Ag/Bi_2O_3 heterostructures modified up-conversion nanoparticles

Shengzhe Zhao [a,1], Yi Yang [a,1], Ran Lu [a], Yan Wang [a], Yun Lu [b,*], Raul D. Rodriguez [c], Evgeniya Sheremet [c], Jinju Chen [a,*]

[a] School of Materials and Energy, University of Electronic Science and Technology of China, Chengdu 610054, PR China
[b] School of Electronic Science and Engineering, University of Electronic Science and Technology of China, Chengdu 610054, PR China
[c] Tomsk Polytechnic University, Lenina Ave. 30, 634034 Tomsk, Russia

ARTICLE INFO

Editor: Dr. GL Dotto

Keywords:
Bi_2O_3
Up-conversion nanoparticles
Selective adsorption
Photocatalytic degradation
Sunlight

ABSTRACT

The degradation of organic pollutant by photocatalytic technology is an emerging and effective approach to purify water resources. Herein, we reported a heterostructure with selective adsorption and photocatalysis for the efficient removal of organic pollutant. The photocatalyst was comprised of up-converting nanoparticle (UCNP) coated with Ag/Bi_2O_3. The specific crystallinity of Bi_2O_3 facilitated the selective adsorption of organic molecules with negative polarity, Ag nanoparticles loaded on Bi_2O_3 promoted the visible light absorption, and the up-conversion property of UCNP turned near-infrared light into ultraviolet and visible light improving further light-harvesting efficiency in the whole solar spectrum. The adsorption process for organic pollutants over $Ag/UCNP@Bi_2O_3$ obeyed the pseudo-second-order and the Langmuir isotherm models, and the maximum Langmuir adsorption capacity for tetracycline reached to 717.4 mg/g at pH 7. Meanwhile, the photocatalytic degradation rate of $Ag/UCNP@Bi_2O_3$ for tetracycline (100 mg/L) achieved to 0.0037 min^{-1} under Xenon lamp irradiation after the adsorption equilibrium. This study provided a feasible strategy to develop photocatalysts with efficient adsorption and photocatalytic ability for organic pollutant from water.

1. Introduction

Photocatalysis is identified as one of the most promising technologies for solving the energy shortage and environmental pollution by directly utilizing solar energy [1–3]. Many nanoscale semiconductor photocatalysts have been researched for the removal of organic pollutants, owning to their high efficiency, low cost, and low secondary pollution [4–6]. However, many challenges remain restricting the development of photocatalysts, including narrow photo-response spectral range, the high recombination rate of photogenerated electron/hole pairs, and poor chemical and thermal stability [7–9]. Therefore, modification of traditional photocatalyst to overcome these problems is becoming a focus of research [10–12]. Compared with the large bandgap semiconductor materials (such as ZnO and TiO_2), the photocatalysts with narrow bandgap can be excited by visible light and achieve higher solar energy utilization efficiency [13–16]. Especially, bismuth oxide (Bi_2O_3) is considered to be an excellent photocatalyst, which is non-toxic, earth-abundant, low cost, and high chemical stability [17–19]. It is found that the physical properties (such as bandgap, surface energy, and zeta potential) strongly depend on the crystal phase that includes four crystalline phases α, β, γ or δ-Bi_2O_3 with a bandgap of 2.6–3.9 eV [20–22]. In addition, the particular orbital hybridization of Bi 6 s and O 2p in Bi_2O_3 makes the valence band (VB) move up, which is helpful for electron transition from VB to the conduction band (CB). This band alignment is beneficial for specific photocatalytic reactions such as carbon dioxide reduction [23–25]. Therefore, it is of great significance to explore new systems that provide Bi_2O_3 higher sunlight utilization efficiency and enhance charge separation.

Semiconductors combined with noble metals (such as Au, Ag, and Pt) form heterostructures that can significantly improve light response due to the excitation of localized surface plasmon resonance (LSPR) of noble metal nanoparticles [26,27]. The small-size noble-metal nanoparticles can also work as active reaction sites and electron traps [27–29]. Since electron transfer occurs at the interface between the semiconductor and the noble metals, their contact areas significantly influence the overall photochemical activity of the heterostructure [26,30]. Therefore, the

* Corresponding authors.
E-mail addresses: luyun1501@uestc.edu.cn (Y. Lu), jinjuchen@uestc.edu.cn (J. Chen).
[1] Shengzhe Zhao and Yi Yang contribute to the work equally.

https://doi.org/10.1016/j.jece.2021.107107
Received 29 October 2021; Received in revised form 18 December 2021; Accepted 27 December 2021
Available online 30 December 2021

coupling between noble-metals and semiconductors is becoming a new way to reduce the recombination rate of charge carriers and improve the harvesting efficiency of visible light.

The photocatalyst system that is only driven by UV and visible light is unable of utilizing solar energy adequately since the near-infrared (NIR) light making up about 46% of the whole solar spectrum gets wasted. However, only a few works about NIR light-driven photocatalysis were reported in the last couple of years [31–33]. Up-conversion materials attracted extensive attention due to their unique properties associated with anti-Stokes scattering. The absorption of low-energy photons generates excited electrons that subsequently transfer to another species resulting in the emission of higher energy photons [34,35]. One of the most striking approaches is up-conversion materials doped with lanthanide, which can convert two or more NIR photons to UV or visible light emissions and further excite the photocatalyst [36–38]. Meanwhile, the core/shell structure consists of semiconductors deposited on the surface of up-conversion materials and can exhibit higher energy transfer efficiency than homogeneous mixtures. This higher performance is because of an efficient luminescence resonance energy transfer (LRET) process occurring when the two materials are in close contact (<10 nm) with each other [37,39].

Herein, a heterostructure was designed to remove organic pollutants efficiently and sufficiently utilize the sunlight for degradation. We selected $NaYF_4$: 10%Yb encapsulated $NaYF_4$: 20%Yb, 0.2%Tm (abbreviated as UCNP) nanoparticle as the core structure, which showed outstanding up-conversion efficiency in terms of UV and blue emissions upon NIR light (980 nm) excitation [40]. Ag/Bi_2O_3 heterostructure was loaded on the surface of UCNP as the shell structure by solvothermal method followed by a photoreduction step. The Bi_2O_3 with specific crystallinity facilitated the selective adsorption for the negative polarity organic molecule; the LSPR effect between Ag and Bi_2O_3 promoted visible light adsorption, and the up-conversion effect of UCNP converting NIR into visible light further improved the light utilization. The Ag/UCNP@Bi_2O_3 presented efficient selective adsorption and photocatalytic activity for tetracycline (TC) removal. This work provides a feasible strategy to design photocatalysts with selective adsorption and photocatalytic activity for organic pollutants under the full solar spectrum.

2. Experimental

The detailed materials (S1.1), synthetic process, characterizations and performance test of photocatalysts could be found in Supplementary Information.

2.1. Preparation of photocatalysts

UCNP were prepared by thermal decomposition method, and Ag/Bi_2O_3 heterojunction were synthesized by solvothermal method combined with photoreduction method. The detailed procedures for the preparation of photocatalysts was displayed in Supplementary Information (S1.2).

2.2. Adsorption activity measurement

The negative polarity methyl orange (MO), the amphoteric tetracycline (TC) and the positive polarity rhodamine B (RhB) were used in this work as the simulated organic pollutants to measure the adsorption performance of the as-prepared samples. The detailed procedure of adsorption activity measurement was exhibited in the Supplementary Information (S1.3).

2.3. Photocatalytic activity measurement

Photocatalytic activities of the as-prepared samples were evaluated by the degradation of the RhB and TC solution. The simulated sunlight was supplied by a Xenon lamp (BL-GHX-V, 300 W), which was equipped with various filters to provide different irradiation bands. In a typical experiment, 40 mL of RhB (10 mg/L) was loaded in a 100 mL quartz reactor. Next, 20 mg of photocatalyst was added to the solution and stirred for 2 h in the dark to reach an adsorption-desorption equilibrium. After that, the solution was exposed to Xenon lamp irradiation for a given time period. The real-time concentration of dye molecules in the solution was calculated according to the Beer-Lambert law using UV–Vis spectroscopy. The RhB degradation process was monitored by the C_t/C_0 ratio, where C_0 was the initial concentration of organic pollution, C_t was the concentration at the time t. The degradation process of TC was similar to the RhB, difference is the concentration of TC (40 mL, 100 mg/L) and weight of the photocatalyst (40 mg) has been adjusted appropriately to achieve the best performance.

2.4. Detection on species of photogenerated ROS

The active species trapped experiments were performed to analyze the photocatalytic mechanism of Ag/UCNP@Bi_2O_3. RhB solution containing 1 mM of 1,4-benzoquinone (BQ), tert-butyl alcohol (*t*-BuOH), or disodium ethylenediaminetetraacetate (Na_2EDTA), was introduced into catalysis solution as the scavenger of superoxide radical ($\bullet O_2^-$), hydroxyl radical (•OH) and hole (h^+), respectively. This experiment was carried out under the same conditions as RhB photodegradation (discussed in 2.3).

3. Results and discussion

3.1. Synthetic strategy

The synthetic process for the core-shell Ag/UCNP@Bi_2O_3 NPs is shown in Fig. 1A. The uniform $NaYF_4$: 20%Yb, 0.2%Tm nanoparticles (Fig. 1A(a)) are synthesized from the thermal decomposition process in organic solvents, and the OA ligands coating on their surface can keep them dispersed in organic solvents (corresponding to Fig. B). The outer layer of $NaYF_4$: 10%Yb is then produced in a process similar to that of $NaYF_4$: 20%Yb, 0.2%Tm to form the UCNP (Fig. 1A(b)), for further enhancing the up-conversion luminescence effect under 980 nm laser irradiation. HCl aqueous solution (pH = 4) is used to protonate the carboxylate groups of OA molecules and remove them from the UCNP for the smooth growth of Bi_2O_3 nanocrystal. Bi_2O_3 is synthesized by the solvothermal method to obtain the UCNP@Bi_2O_3 core-shell structure (Fig. 1A(c)). Ethylene glycol (EG) is chosen to dissolve $Bi(NO_3)_3{\cdot}5H_2O$ and maintain the stable morphology of UCNP. The chemical reaction in the process to obtain Bi_2O_3 nanoparticles can be formulated as in Fig. 1A (e). Ag NPs are loaded onto the core-shell structure's surface by the photoreduction of $AgNO_3$ under the simulated sunlight conditions to form the Ag/UCNP@Bi_2O_3 (Fig. 1A(d)).

3.2. Characterization

The morphology of the as-prepared samples was characterized by TEM as shown in Fig. 1B-E. The $NaYF_4$: 20%Yb, 0.2%Tm (Fig. 1B), and the UCNP (Fig. 1C) both display uniform spherical appearance, which is the characteristic morphology of $NaYF_4$ crystals as reported in previous work [35]. And the size of the UCNP with an average diameter of about 20 nm is larger than that of the $NaYF_4$: 20%Yb, 0.2%Tm. After the solvothermal reaction, a rough shell with a thickness of about 2 nm composed of small Bi_2O_3 nanodots is grown on the surface of the UCNPs to form the UCNP@Bi_2O_3 core-shell nanostructure (Fig. 1D). The change of samples was analyzed by particle size diagram shown in Fig. S1 in Supplementary Information. The morphology of the UCNP@Bi_2O_3 is not significantly changed after the modification with Ag NPs by the photoreduction process as shown in Fig. 1E, which may be owing to the small size and the low content of Ag NPs. The HRTEM image (inset in Fig. 1E) exhibits two distinct lattice fringes with a spacing of ~0.52 nm

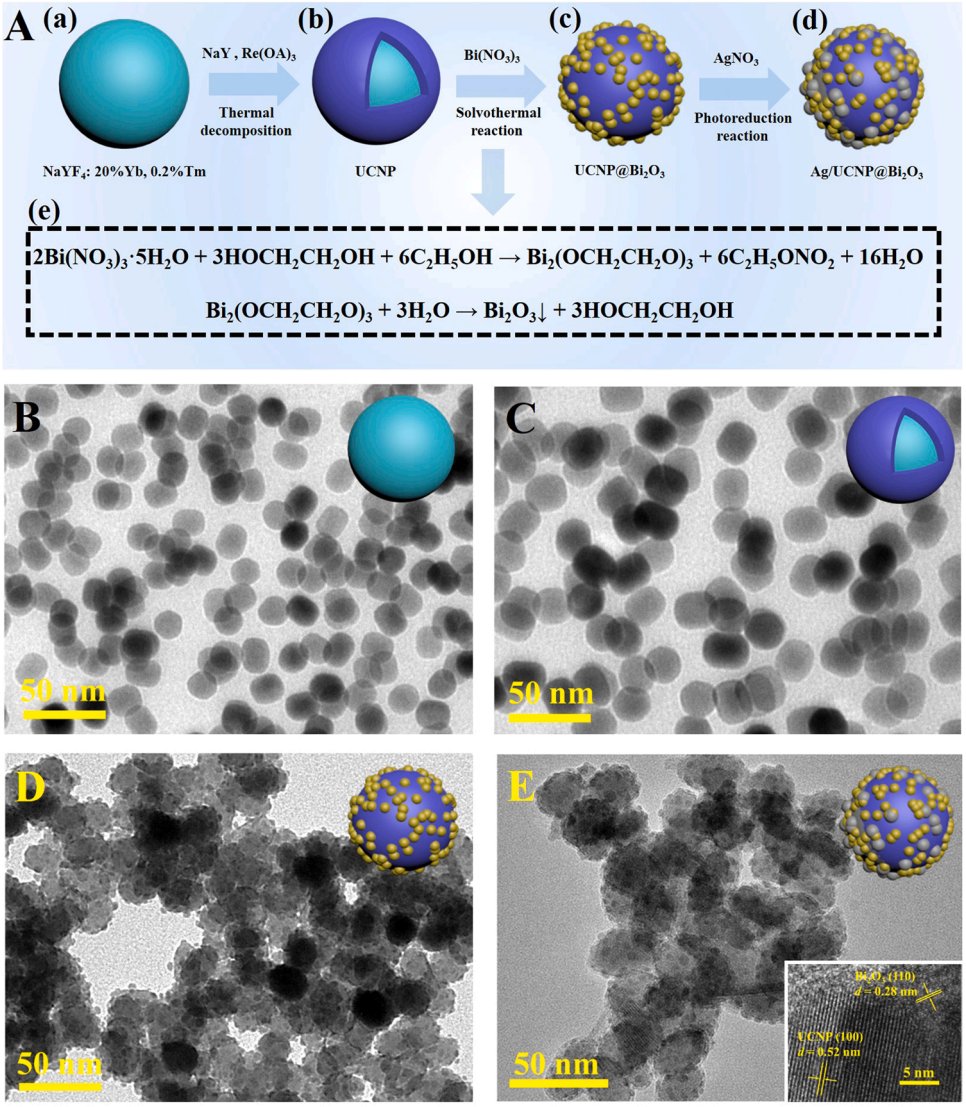

Fig. 1. The synthesis diagram of Ag/UCNP@Bi_2O_3 nanoparticle (A). The typical TEM images of $NaYF_4$: 20%Yb, 0.2%Tm (B), UCNP (C), and UCNP@Bi_2O_3 (D). The TEM image of Ag/UCNP@Bi_2O_3 and the HRTEM image (inset) (E).

corresponding to the (100) plane of $NaYF_4$ and a larger spacing of ~0.28 nm corresponding to the (110) plane of Bi_2O_3. These results confirm that the structures are crystalline, in agreement with the XRD results in Fig. 2A. Energy dispersive spectroscopy (EDS) was used to verify the elemental composition of Ag/UCNP@Bi_2O_3. As shown in Fig. S2 in Supplementary Information, elemental Bi, O, Na, Y, and F can be observed, while there is overlap between the Bi and Y peaks, leading to higher atomic ratio analysis error. Although weak, the Ag peak is present, indicating that the modification with Ag NPs through photoreduction was successful.

The crystalline structures of the UCNP and the Ag/UCNP@Bi_2O_3 were confirmed by the XRD patterns (Fig. 2A). All of the diffraction peaks from primitive UCNP (black line) can be clearly indexed to pure hexagonal β-phase $NaYF_4$ crystal (JCPDS no. 16-0334). The peaks located at 17.2°, 30.1°, 30.7°, 43.5°, and 53.7° are consistent with the (100), (110), (101), (201), and (211) planes of β-$NaYF_4$ crystal, respectively. After the modification of Bi_2O_3 and Ag NPs, the XRD pattern of the Ag/UCNP@Bi_2O_3 (red line) shows an almost amorphous structure and only faint β-Bi_2O_3 peaks can be observed except UCNP. The peaks at 28.8°, 32.6°, 46.14°, and 55.6° are well indexed to the β-Bi_2O_3 (JCPDS no. 27-0050), suggesting that Bi_2O_3 exists in a heterogeneous structure consisting of mainly amorphous and a small amount of tetragonal phase. There are no pronounced diffraction peaks from Ag in the Ag/UCNP@Bi_2O_3, probably due to the low mass ratio of Ag and Bi_2O_3, and the loaded Ag with small size that the peaks are hard to be detected. Therefore, the XRD analysis confirms our expectation that the Ag/UCNP@Bi_2O_3 comprises an amorphous/tetragonal phase Bi_2O_3 and the hexagonal phase $NaYF_4$, which will facilitate the selective adsorption of organic pollutants and the full utilization of the solar spectrum for catalytic degradation.

The surface elements and chemical states of the Ag/UCNP@Bi_2O_3 were analyzed by XPS. The Bi, O, Ag, C, F, and Y peaks can be observed in the spectrum in Fig. 2B. The high-resolution XPS spectrum of Bi 4f (Fig. S3A) has two different peaks at 157.98 eV and 163.32 eV, which are attributed to Bi $4f_{7/2}$ and Bi $4f_{5/2}$, respectively. The difference value of the Bi 4f peaks is 5.3 eV which is consistent with the Bi_2O_3 form [1]. Similarly, the different peaks at 302.27 eV and 314.0 eV in Fig. S3B are attributed to Y $3p_{3/2}$ and Y $3p_{1/2}$, which demonstrates the Y presence in the form $NaYF_4$. The Ag $3d_{5/2}$ and Ag $3d_{3/2}$ peaks at 368.01 eV and 373.91 eV are ascribed to Ag^0 as shown in Fig. S3C, which shift down by 0.19 eV compared to pure Ag with peaks at 368.2 eV and 374.1 eV [30]. The binding energy shift of Ag 3d to Bi 4f indicates that the Ag NPs were successfully loaded on the surface of Bi_2O_3 to form the Ag/Bi_2O_3 heterostructure.

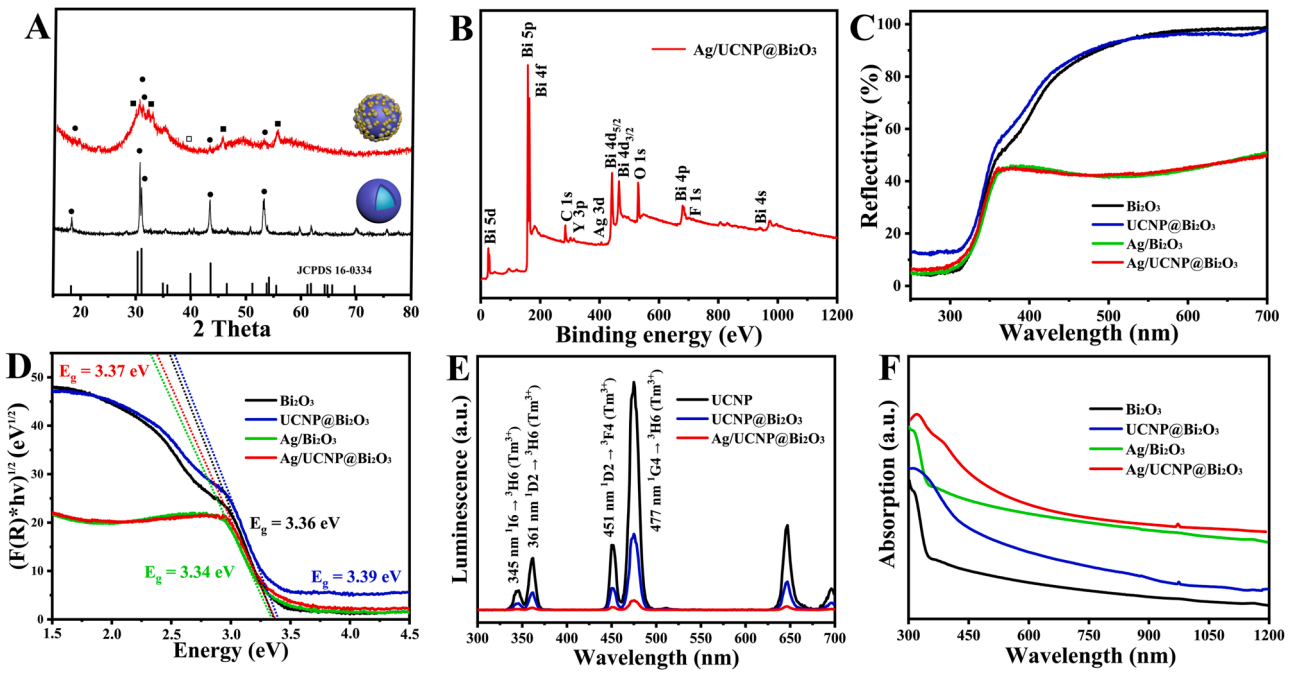

Fig. 2. The XRD patterns (A) of the UCNP and the Ag/UCNP@Bi_2O_3. The XPS spectrum of the Ag/UCNP@Bi_2O_3 (B). The DRS spectrum of the as-prepared samples (C), and the derived bandgap energy (D). The PL spectra (E) and the UV–Vis–NIR absorption spectra (F) of samples. (For interpretation of the references to colour in this figure, the reader is referred to the web version of this article.)

The photocatalytic capacity of the Ag/UCNP@Bi_2O_3 is related to the degree of light absorption. Therefore, the UV–Vis DRS was tested to determine the optical properties of the as-prepared samples. The typical reflectance spectrum of pure Bi_2O_3 can be observed in Fig. 2C, which means the good visible light absorption of the as-prepared Bi_2O_3. The DRS of UCNP@Bi_2O_3 does not change significantly from that of Bi_2O_3, indicating that the UCNP has nearly no effect on the UV–Vis absorption of the sample. As for the Ag/Bi_2O_3 and Ag/UCNP@Bi_2O_3, the overall intensity of visible light reflection is further reduced compared with that of the Bi_2O_3 and UCNP@Bi_2O_3. These results confirm that the heterojunction and the LSPR effect between Ag and Bi_2O_3 enhance their visible light absorption efficiency. The bandgap energies of the as-prepared samples are obtained from DRS spectra by applying the Kubelka-Munk function as shown in Fig. 2D. The UCNP is not a semiconductor material. As a result, the bandgap of the UCNP@Bi_2O_3 becomes larger, which also could explain the increase of Ag/UCNP@Bi_2O_3. Meanwhile, Ag could facilitate the electron transfer of semiconductors, and lead to the bandgap of the Ag/Bi_2O_3 decline. This could explain the decrease of the Ag/UCNP@Bi_2O_3 bandgap relative to the UCNP@Bi_2O_3.

Fig. 2E shows the photoluminescence (PL) spectrum of the as-prepared samples under the excitation of a 980 nm NIR laser. The UCNP displays two UV emission bands at 345 nm and 361 nm and two visible (blue) emissions at 451 nm and 477 nm, which are due to the transitions of $^1I_6 \rightarrow {}^3H_6$, $^1D_2 \rightarrow {}^3H_6$, $^1D_2 \rightarrow {}^3F_4$, and $^1G_4 \rightarrow {}^3H_6$ in Tm^{3+} ions, respectively. After being loaded with the Bi_2O_3 shell, the intensities of UV and visible emissions drastically declined, which means that the LRET process may occur in the UCNP@Bi_2O_3 hybrid nanostructure, leading to a more efficient energy transfer. Generally speaking, the strong fluorescence intensities in PL spectrum indicates the high recombination of photogenerated electron-hole pairs. The fluorescence intensity of the Ag/UCNP@Bi_2O_3 was slight, meaning the minimum recombination rate of photogenerated carriers. The UV–Vis–NIR absorption spectrum of the as-prepared samples is presented in Fig. 2F. The strong absorption peaks in the UV and visible region corresponding to the excitation process of the Ag/Bi_2O_3 heterostructure. The weak peak at 980 nm can be attributed to the up-conversion process of UCNP. The combination of all these absorption characteristics into a system presents the possibility of a broad photo-response from the UV to NIR range.

3.3. Adsorption and photocatalytic activity

As common simulated pollutants, MO and RhB were used to evaluate the adsorption and photocatalytic performance of the as-prepared photocatalysts under simulated solar source (Xenon lamp, wavelength: 200–1000 nm). The MO (40 mL, 10 mg/L) solution with the photocatalysts (40 mg) was magnetically stirred in the dark to achieve the adsorption/desorption equilibrium and minimize the effect of adsorption kinetics on the photodegradation evaluation. Surprisingly, the MO molecule is almost entirely absorbed by the four types of nanoparticles in less than 1 h (Fig. 3A). This phenomenon may be caused by the electrostatic interaction between the high positive potential caused by the special Bi_2O_3 crystallinity and the negative potential of the MO molecule. The special crystalline Bi_2O_3 we prepared in the research is the compound of amorphous structure and faint β-Bi_2O_3. Amorphous Bi_2O_3 molecules may contain a large number of dangling bonds, which endows Bi_2O_3 more active adsorption capacity. In contrast, the photocatalysts (40 mg) show relatively weak adsorption to positive polarity RhB (40 mL, 10 mg/L), and the adsorption process is unstable, accompanied by the desorption process as shown in Fig. 3B. The concentration of the simulated pollutants decreases during adsorption process, resulting in the electrostatic interaction variable, and thus leading to the adsorption efficiency unstable.

The zeta potential and the adsorption of the as-prepared photocatalysts at different temperatures were obtained to verify this hypothesis. The samples' zeta potential results obtained at pH = 7 are shown in Fig. 3C. All samples show a positive potential, but the values for the Ag/UCNP@Bi_2O_3 and the UCNP@Bi_2O_3 are remarkably higher. The pH_{zpc} value of the Ag/UCNP@Bi_2O_3 was measured to be 11. In the case of pH < pH_{zpc}, the surface of the Ag/UCNP@Bi_2O_3 is positively charged due to the formation of H_3O^+, leading to an enhancement of adsorption capacity to negative polarity molecule. The zeta potential depends on the environment temperature. With the temperature rising above 25 °C, the photocatalysts adsorption efficiency to RhB after 2 h presents a

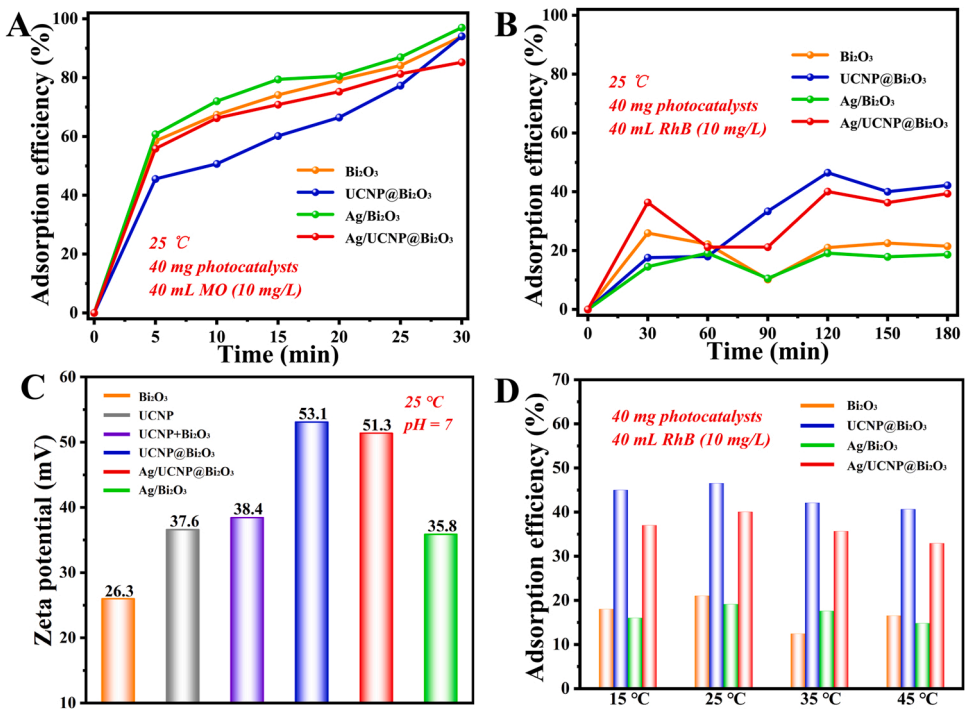

Fig. 3. MO (A) and RhB (B) adsorption to the as-prepared photocatalysts. The zeta potentials of the corresponding nanoparticles (C). The adsorption effect of the photocatalysts to RhB taking 2 h at different temperatures (D).

downtrend as shown in Fig. 3D, further confirming that the adsorption process is related to the samples' potential [7].

To further test the selective adsorption property of the photocatalysts, the adsorption of high concentration MO (250 mg/L) and RhB (100 mg/L) were considered. The adsorption curves of different samples exhibit a similar trend in Fig. 4A, and all the samples show excellent adsorb ability with more than 80% adsorption rate within 8 h. The corresponding pseudo-first-order and pseudo-second-order kinetic models are presented in Fig. 4B and C, respectively. The adsorption model of all photocatalysts is more consistent with the pseudo-second-

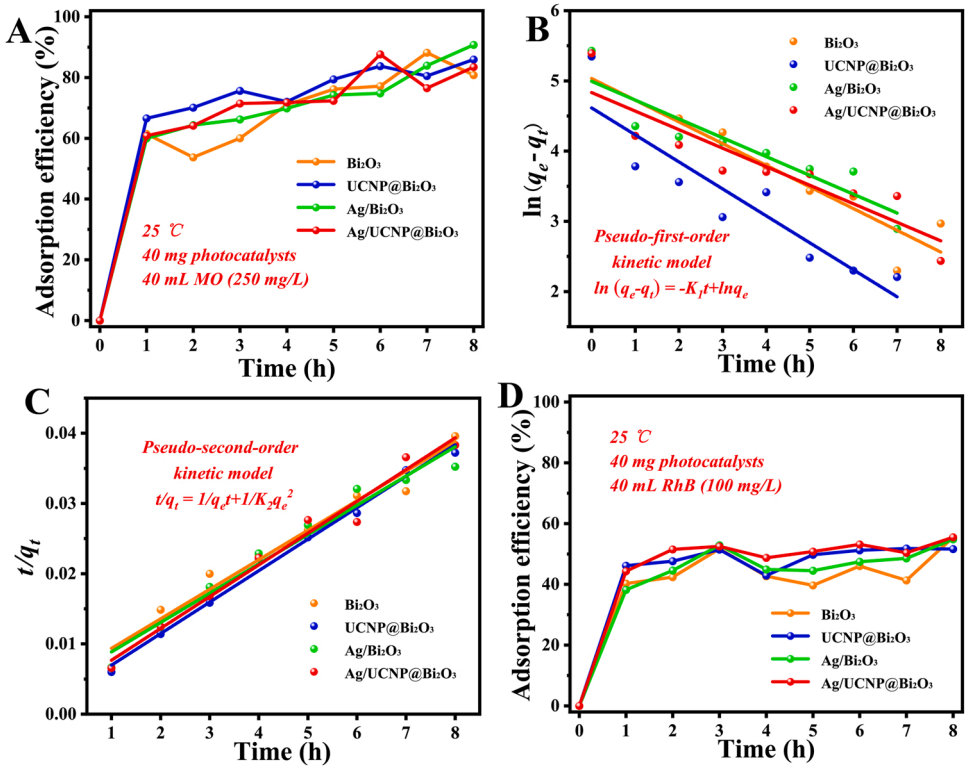

Fig. 4. High concentration MO adsorption on the as-prepared photocatalysts (A). The corresponding pseudo-first-order kinetic model (B) and pseudo-second-order kinetic model (C). The adsorption effect of the as-prepared photocatalysts to the high concentration RhB (D).

order kinetics (R^2 = 0.972) rather than the pseudo-first-order (R^2 = 0.835), suggesting that the adsorption process comes from potential action and specific surface area adsorption. The adsorption efficiency of the samples to high concentration RhB (100 mg/L) (Fig. 4D) shows a similar trend with that of the low RhB concentration (10 mg/L). The photocatalysts' adsorption effect to high RhB concentration is worse than that of the high MO concentration, implying the selective photocatalysts' adsorption capacity.

To better present the photodegradation property of the samples, we selected the positive polarity dyes RhB (40 mL, 10 mg/L) as simulated organic pollutants and reduced the quality of the sample (20 mg) to lower the adsorption. After reaching the adsorption/desorption equilibrium in the dark, the photocatalytic activity of the samples was investigated under Xenon lamp irradiation. Fig. 5A shows the concentration change curves of RhB during photodegradation. After Xenon lamp irradiation without optical filter for 5 min, Ag/UCNP@Bi_2O_3 shows excellent photocatalytic activity (87.1%), much higher than the Ag/Bi_2O_3 (63.7%) and the UCNP@Bi_2O_3 (44.7%). The catalytic performance of Bi_2O_3 is average (37.6%), and the RhB concentration without photocatalyst remained unchanged under illumination. The Ag NPs on Bi_2O_3 can work as the active sites to improve the light absorption efficiency due to LSPR excitation. Meanwhile, the Ag NPs load can decrease the recombination rate of the photogenerated electrons and holes to further increase the photocatalytic activity. Therefore, the photocatalytic performance of samples is significantly enhanced after Ag NPs loading. The Xenon lamp used in this experiment contains UV, visible, and NIR light. Thus, the difference in photocatalytic activity between the Ag/UCNP@Bi_2O_3 and the Ag/Bi_2O_3 (similar as the UCNP@Bi_2O_3 and the Bi_2O_3) can be inferred from the up-conversion effect of UCNP, which improves the light utilization and extend the excitation light range of photocatalyst.

To evidence the photocatalytic capacity of samples under NIR light irradiation, the photocatalytic degradation was investigated using a Xenon lamp with filters to block the high energy spectral range (UV and visible) except for NIR light that passed through (main band $\lambda = 980$ nm) [39]. As shown in Fig. 5B, after equilibrium, the RhB degradation barely changed by Bi_2O_3 and Ag/Bi_2O_3, with a slight RhB desorption observed for Bi_2O_3 due to the temperature increase caused by NIR light. In contrast, a significant RhB concentration decrease is observed in the case of UCNP@Bi_2O_3 or Ag/UCNP@Bi_2O_3. Remarkably, the Ag/UCNP@Bi_2O_3 (56.3%) nanostructure exhibits higher catalytic activity than the UCNP@Bi_2O_3 (42.5%) after 120 min of reaction. From the kinetics point of view, the photodegradation process can be considered as a first-order reaction, and the degradation rate can be expressed as $\ln(C_0/C_t) = kt$, where k is the degradation rate constant (min^{-1}). The rate constant values were determined from the slope of $\ln(C_0/C_t)$ versus t plots. As shown in Fig. 5D, the Ag/UCNP@Bi_2O_3 shows high photocatalytic activity with a rate constant (k) of 0.0051 min^{-1}, much higher than that of the UCNP@Bi_2O_3 (0.0036 min^{-1}), the Ag/Bi_2O_3 (0.0012 min^{-1}), and the Bi_2O_3 (0.0006 min^{-1}). In addition, we also investigated the photocatalytic stability of the Ag/UCNP@Bi_2O_3 under Xenon lamp irradiation. Our results show that the nanostructure exhibits good stability after being reused five times (Fig. 5E).

To better understand the photocatalytic process, the different reactive oxygen species ($\bullet O_2^-$, •OH, h^+) generated during the photocatalytic process were identified by free radical and hole scavenging experiments. RhB solution containing 1 mM of 1,4-benzoquinone (BQ), tert-butyl alcohol (*t*-BuOH), or disodium ethylenediaminetetraacetate (Na_2EDTA), was introduced into the catalysis solution as scavengers of $\bullet O_2^-$, •OH and h^+, respectively. This experiment was carried out under the same conditions as RhB photodegradation. Fig. 5F shows the photodegradation of RhB by the Ag/UCNP@Bi_2O_3 in the presence of these various ROS probe compounds under Xenon lamp illumination. Compared with the no scavenger system, the reaction in the presence of the •OH scavenger *t*-BuOH is slightly slower. In contrast, the reaction performed in the presence of the h^+ scavenger Na_2EDTA is nearly completely inhibited. The photocatalytic activity is also greatly reduced in the presence of the $\bullet O_2^-$ scavenger BQ. These results strongly suggest that $\bullet O_2^-$, •OH, and h^+ all contribute to the photodegradation, but •OH radical is the key intermediate as its trapping results in complete suppression of catalytic activity.

For exploring the adsorption and photocatalytic capacity of Ag/UCNP@Bi_2O_3 in practical application, we chose tetracycline (TC) as targeted pollutant, which is a common antibiotic and difficult to be removed in natural conditions. The effect of initial TC concentration on the adsorption by Ag/UCNP@Bi_2O_3 was studied (Fig. 6A), and the data

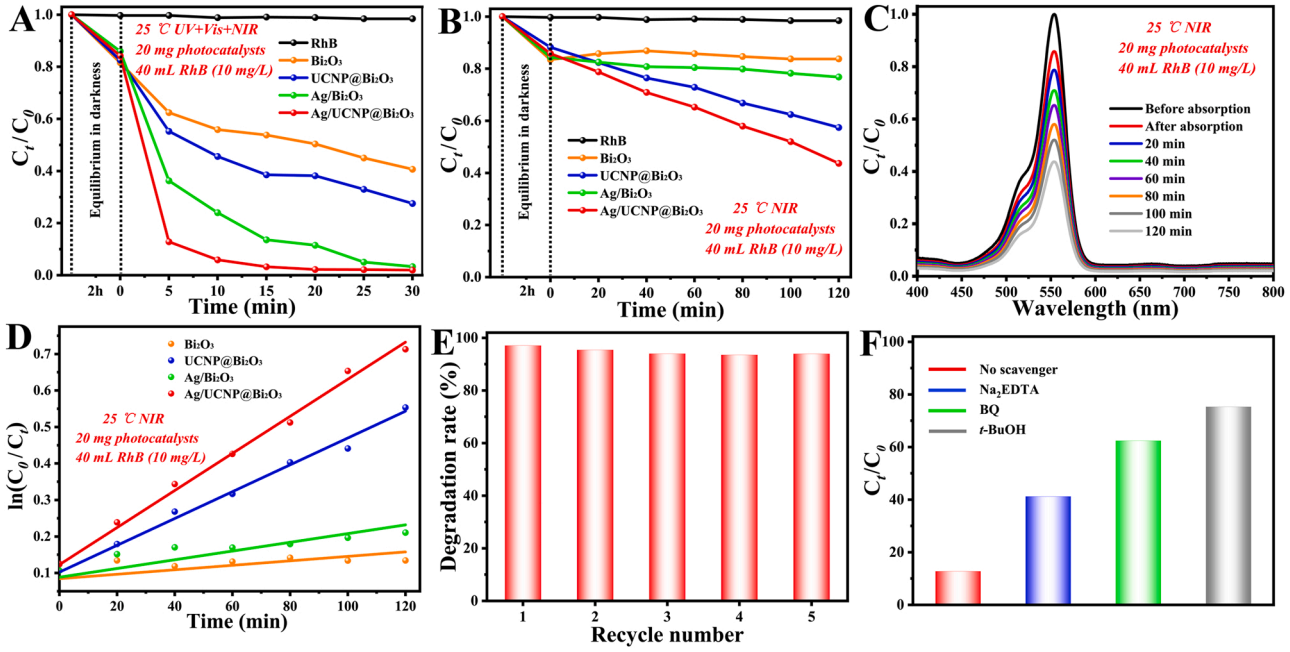

Fig. 5. The photodegradation activity of the as-prepared photocatalysts to RhB under full-range light (A), and NIR light (B). The UV–Vis absorption spectra of RhB over Ag/UCNP@Bi_2O_3 under NIR light (C). The fitted curve of photodegradation activity under NIR light (D). Photodegradation activity of five cycles under full-range light (E). The photocatalytic activity of the Ag/UCNP@Bi_2O_3 with scavenger under the Xenon lamp radiation for 5 min (F).

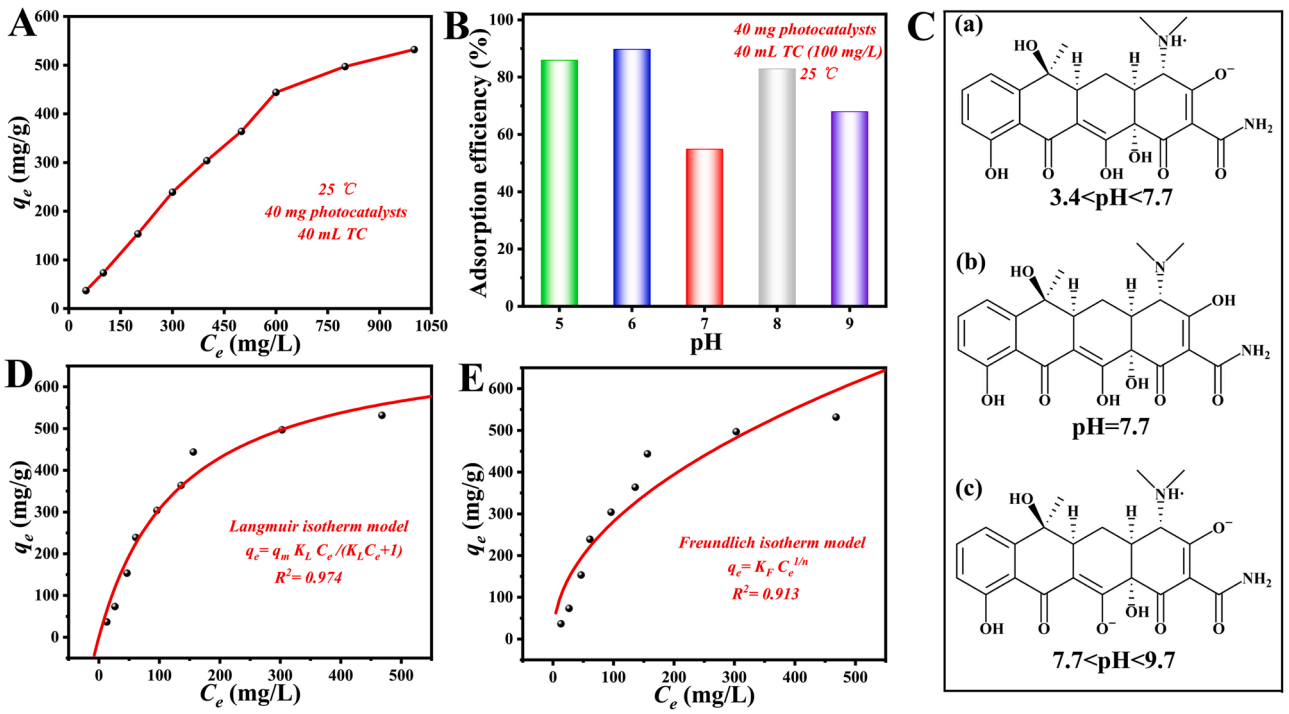

Fig. 6. The effect of initial TC concentration on the adsorption by Ag/UCNP@Bi_2O_3 (A). The effect of initial pH value of TC solution on the adsorption property of Ag/UCNP@Bi_2O_3 (B). The molecular formula of TC at different pH (C). The Langmuir adsorption isotherm (D) and the Freundlich adsorption isotherm (E) of TC by Ag/UCNP@Bi_2O_3.

were analysed using the Langmuir (Fig. 6D) and the Freundlich (Fig. 6E) isotherm models. The result was better described by the Langmuir model based on its higher coefficient of determination (R^2 = 0.974, q_m=717.4 mg/g), which indicated the adsorption of TC onto Ag/UCNP@Bi_2O_3 transpired via monolayer adsorption. Meanwhile, the influence of initial pH value of the TC solution on the adsorption capacity of Ag/UCNP@Bi_2O_3 was explored. As shown in Fig. 6B, the adsorption rate of the samples increased in both acid and alkali conditions, and showed the highest adsorption rate at the pH= 6 condition. This phenomenon can be explained by the molecular formula of TC at

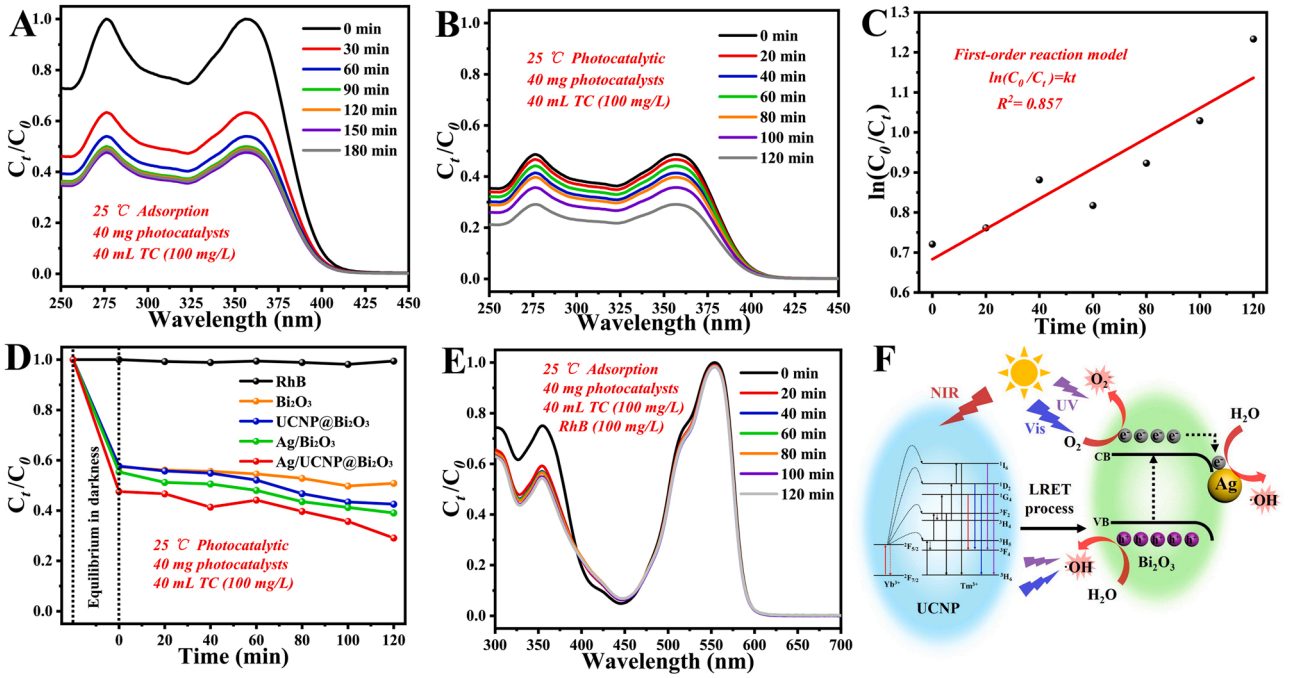

Fig. 7. The UV–Vis absorption spectra of TC over Ag/UCNP@Bi_2O_3 with different time under dark adsorption conditions (A) and photodegradation of TC under full range Xenon lamp illumination (B). The fitted curve of photodegradation of TC over Ag/UCNP@Bi_2O_3 under full range Xenon lamp illumination (C). The photodegradation activity of the as-prepared photocatalysts to TC under full-range light (D). The selective adsorption capacity of the Ag/UCNP@Bi_2O_3 for the mixed solution of TC and RhB (E). The schematic illustration of the photocatalytic mechanism of the Ag/UCNP@Bi_2O_3, and the energy transfer mechanisms show the up-conversion process of Yb^{3+} and Tm^{3+} doped UCNPs under 980 nm excitation (F).

different pH (Fig. 6C). The TC is an amphoteric molecule, which could occur dissociation either acid or alkali conditions as shown in Fig. 6C, leading to the decrease of potential. This phenomenon enhanced the interaction between TC molecule and Ag/UCNP@Bi_2O_3, and thus enhances the increase of adsorption rate.

Then, we chose the TC solution in suitable concentration (100 mg/L) to further verify the photodegradation ability. After reaching the adsorption/desorption equilibrium in dark, the Ag/UCNP@Bi_2O_3 was subsequently irradiated under the full spectrum Xenon lamp illumination, for investigating the adsorption and photocatalytic activity. The TC removal processes by the Ag/UCNP@Bi_2O_3 were shown in Fig. 7A (dark) and B (light), respectively. From the time-dependent absorbance of TC solution over the Ag/UCNP@Bi_2O_3, the intrinsic peak of TC molecules at 356 nm gradually decreases with the reaction time. The Ag/UCNP@Bi_2O_3 was found a good adsorption amount for TC, which could adsorb 53% TC within 90 min in dark. Besides, under full spectrum light irradiation, the Ag/UCNP@Bi_2O_3 showed excellent photodegradation effect accompanying mild desorption, and the degradation rate for TC (100 mg/L) could reach to 0.0037 min^{-1} by the first-order reaction model (Fig. 7C). On the contrary, when the special crystalline Ag/UCNP@Bi_2O_3 has been calcined at 450 ℃ for 1 h, its adsorption and photocatalytic capacity both decreased (Fig. S4), which meant the special crystalline sample showing better removal effect for the organic pollutant. The photodegradation trend of the as-prepared samples to TC (Fig. 7D) is the same as that to RhB, indicating the degradation process is universal. The mixed solution of TC and RhB with equal concentration (100 mg/L) was used to verify the selective adsorption of the Ag/UCNP@Bi_2O_3. As shown in Fig. 7E, the peak (356 nm) of TC in the UV–Vis absorption spectra showed an obvious downward trend with time changing. While the peak (550 nm) of RhB in the mixed solution almost unchanged, indicating the Ag/UCNP@Bi_2O_3 has selective adsorption capacity.

3.4. Mechanism for the enhancement of photocatalytic activity

Under excitation by NIR light, the UCNP absorbs NIR photons, the electrons in Tm^{3+} ions get excited to high energy levels, and then NIR light is upconverted to UV and visible light. The excited electrons in the UCNP may transfer to the surrounding of the Ag/Bi_2O_3 shell via an efficient LRET process. This transfer process can better utilize the excited electrons than a single radiation reabsorption process (Fig. 7F). Therefore, the Ag/Bi_2O_3 heterostructure is activated by the UCNP under NIR light and sequentially produces photogenerated (PG) e^- and h^+. Meanwhile, the local surface plasmon resonance (LSPR) effect caused by the Ag nanoparticles could cause electron oscillation to facilitate the charge carriers transfer, which is an effective strategy to promote the separation efficiency of photoexcited charge carriers [41–45]. When the PG e^- migrates to the particle surface, it reacts with surrounding O_2 and produces $\bullet O_2^-$ radicals that act as oxidants for the dye degradation. On the other hand, due to the unique band structure of the Bi_2O_3 when the PG h^+ migrates to the particle surface, they will directly excite H_2O molecules to form •OH. Besides working under NIR light, the Ag/Bi_2O_3 shell also can be activated by UV and visible light. Therefore, the Ag/UCNP@Bi_2O_3 composites show an enhanced activity under the full solar light.

4. Conclusions

In summary, the Ag/UCNP@Bi_2O_3 composites exhibited efficient selective adsorption and photocatalytic activity for organic pollutant removal. The selective adsorption of the Ag/UCNP@Bi_2O_3 mainly from the specific crystallinity of Bi_2O_3, and the adsorption process for organic pollutants obeyed the pseudo-second-order and the Langmuir isotherm models. The LSPR effect between Ag and Bi_2O_3 promoted visible light adsorption, and the up-conversion effect of UCNP converting NIR into visible light further improved the light utilization. Meanwhile, the reactive oxygen species and photocatalysis pathway were elucidated and discussed in detail. This study provided a new route for developing highly efficient adsorbent and broadband photocatalysts for the removal of organic pollutants from water.

CRediT authorship contribution statement

Sheng-Zhe Zhao: Methodology, Writing – original draft. **Yi Yang**: Visualization. **Ran Lu**: Investigation. **Yan Wang**: Resources. **Yun Lu**: Validation, Project administration. **Raul D. Rodriguez**: Writing – review & editing. **Evgeniya Sheremet**: Formal analysis. **Jin-Ju Chen**: Conceptualization, Supervision.

Declaration of Competing Interest

The authors declare that they have no known competing financial interests or personal relationships that could have appeared to influence the work reported in this paper.

Acknowledgements

This work was funded by Sichuan Science and Technology Program (Grant 2018HH0152, China) and TPU development program (Russia).

Appendix A. Supporting information

Supplementary data associated with this article can be found in the online version at doi:10.1016/j.jece.2021.107107.

References

[1] X. Yang, Y. Zhang, Y. Wang, C. Xin, P. Zhang, D. Liu, B.B. Mamba, K.K. Kefeni, A. T. Kuvarega, J. Gui, Hollow β-Bi_2O_3@CeO_2 heterostructure microsphere with controllable crystal phase for efficient photocatalysis, Chem. Eng. J. 387 (2020), 124100.
[2] W. Wei, Q. Tian, H. Sun, P. Liu, Y. Zheng, M. Fan, J. Zhuang, Efficient visible-light-driven photocatalytic H_2 evolution over MoO_2-C/CdS ternary heterojunction with unique interfacial microstructures, Appl. Catal. B Environ. 260 (2020), 118153.
[3] J.F. Liao, W.Q. Wu, Y. Jiang, J.X. Zhong, L. Wang, D.B. Kuang, Understanding of carrier dynamics, heterojunction merits and device physics: towards designing efficient carrier transport layer-free perovskite solar cells, Chem. Soc. Rev. 49 (2020) 354–381.
[4] X. Lian, W. Xue, S. Dong, E. Liu, H. Li, K. Xu, Construction of S-scheme Bi_2WO_6/g-C_3N_4 heterostructure nanosheets with enhanced visible-light photocatalytic degradation for ammonium dinitramide, J. Hazard. Mater. 412 (2021), 125217.
[5] Y. Chen, R. Yin, L. Zeng, W. Guo, M. Zhu, Insight into the effects of hydroxyl groups on the rates and pathways of tetracycline antibiotics degradation in the carbon black activated peroxydisulfate oxidation process, J. Hazard. Mater. 412 (2021), 125256.
[6] X. Zhang, X. Yuan, L. Jiang, J. Zhang, H. Yu, H. Wang, G. Zeng, Powerful combination of 2D g-C_3N_4 and 2D nanomaterials for photocatalysis: recent advances, Chem. Eng. J. 390 (2020), 124475.
[7] Z. Cheng, S. Zhao, L. Han, A novel preparation method for ZnO/gamma-Al_2O_3 nanofibers with enhanced absorbability and improved photocatalytic water-treatment performance by Ag nanoparticles, Nanoscale 10 (2018) 6892–6899.
[8] S. Zhao, Z. Cheng, L. Kang, M. Li, Z. Gao, The facile preparation of Ag decorated TiO_2/ZnO nanotubes and their potent photocatalytic degradation efficiency, RSC Adv. 7 (2017) 50064–50071.
[9] H. Zhang, Y. Song, L.-c Nengzi, J. Gou, B. Li, X. Cheng, Activation of persulfate by a novel magnetic $CuFe_2O_4$/Bi_2O_3 composite for lomefloxacin degradation, Chem. Eng. J. 379 (2020), 122362.
[10] Z. Cheng, S. Zhao, Z. Han, Y. Zhang, X. Zhao, L. Kang, A novel preparation of Ag@TiO_2 tubes and their potent photocatalytic degradation efficiency, CrystEngComm 18 (2016) 8756–8761.
[11] Z. Cheng, S. Zhao, L. Kang, M. Li, Z. Gao, A novel preparation of hollow TiO_2 nanotubes and pine-cone shaped CdS nanoparticles coated for enhanced ultraviolet and visible light photocatalytic activity, Mater. Lett. 214 (2018) 80–83.
[12] Y. Yan, Z. Zhou, Y. Cheng, L. Qiu, C. Gao, J. Zhou, Template-free fabrication of α- and β-Bi_2O_3 hollow spheres and their visible light photocatalytic activity for water purification, J. Alloy. Compd. 605 (2014) 102–108.
[13] Z. Dai, Y. Zhen, Y. Sun, L. Li, D. Ding, $ZnFe_2O_4$/g-C_3N_4 S-scheme photocatalyst with enhanced adsorption and photocatalytic activity for uranium(VI) removal, Chem. Eng. J. 415 (2021), 129002.
[14] T. Wang, Y. Wang, M. Sun, A. Hanif, H. Wu, Q. Gu, Y.S. Ok, D.C.W. Tsang, J. Li, J. Yu, J. Shang, ZIF8 Thermally treated zeolitic imidazolate framework-8 (ZIF-8) for visible light photocatalytic degradation of gaseous formaldehyde, Chem. Sci. 11 (2020) 6670–6681.

[15] Z. Yi, Y. Cao, J. Yuan, C. Mary, Z. Wan, Y. Li, C. Zhu, L. Zhang, S. Zhu, Functionalized carbon fibers assembly with Al/Bi_2O_3: a new strategy for high-reliability ignition, Chem. Eng. J. 389 (2020), 124254.
[16] G.H. Jeong, S.P. Sasikala, T. Yun, G.Y. Lee, W.J. Lee, S.O. Kim, Nanoscale assembly of 2D materials for energy and environmental applications, Adv. Mater. (2020), e1907006.
[17] Y. Sun, Z. Zhang, A. Xie, C. Xiao, S. Li, F. Huang, Y. Shen, An ordered and porous N-doped carbon dot-sensitized Bi_2O_3 inverse opal with enhanced photoelectrochemical performance and photocatalytic activity, Nanoscale 7 (2015) 13974–13980.
[18] N. Zhu, C. Li, L. Bu, C. Tang, S. Wang, P. Duan, L. Yao, J. Tang, D.D. Dionysiou, Y. Wu, Bismuth impregnated biochar for efficient estrone degradation: The synergistic effect between biochar and Bi/Bi_2O_3 for a high photocatalytic performance, J. Hazard. Mater. 384 (2020), 121258.
[19] L. Zhang, Y. Shi, Z. Wang, C. Hu, B. Shi, X. Cao, Porous β-Bi_2O_3 with multiple vacancy associates on highly exposed active {220} facets for enhanced photocatalytic activity, Appl. Catal. B Environ. 265 (2020), 118563.
[20] Q. Zou, H. Li, Y. Yang, Y. Miao, Y. Huo, Bi_2O_3/TiO_2 photocatalytic film coated on floated glass balls for efficient removal of organic pollutant, Appl. Surf. Sci. 467–468 (2019) 354–360.
[21] J. Divya, N.J. Shivaramu, W. Purcell, W.D. Roos, H.C. Swart, Effects of annealing temperature on the crystal structure, optical and photocatalytic properties of Bi_2O_3 needles, Appl. Surf. Sci. 520 (2020), 146294.
[22] Y. Wang, S. Li, X. Xing, F. Huang, Y. Shen, A. Xie, X. Wang, J. Zhang, Self-assembled 3D flowerlike hierarchical Fe_3O_4@Bi_2O_3 core-shell architectures and their enhanced photocatalytic activity under visible light, Chemistry 17 (2011) 4802–4808.
[23] W. Dou, X. Hu, L. Kong, X. Peng, Photo-induced dissolution of Bi_2O_3 during photocatalysis reactions: mechanisms and inhibition method, J. Hazard. Mater. 412 (2021), 125267.
[24] T. Chen, Q. Hao, W. Yang, C. Xie, D. Chen, C. Ma, W. Yao, Y. Zhu, A honeycomb multilevel structure Bi_2O_3 with highly efficient catalytic activity driven by bias voltage and oxygen defect, Appl. Catal. B Environ. 237 (2018) 442–448.
[25] S. You, Y. Hu, X. Liu, C. Wei, Synergetic removal of Pb(II) and dibutyl phthalate mixed pollutants on Bi_2O_3-TiO_2 composite photocatalyst under visible light, Appl. Catal. B Environ. 232 (2018) 288–298.
[26] M.V. Grabchenko, G.V. Mamontov, V.I. Zaikovskii, V. La Parola, L.F. Liotta, O. V. Vodyankina, The role of metal-support interaction in Ag/CeO_2 catalysts for CO and soot oxidation, Appl. Catal. B Environ. 260 (2020), 118148.
[27] S. Zhao, Z. Cheng, L. Kang, Y. Zhang, X. Zhao, A novel preparation of porous spong-shaped Ag ZnO heterostructures and their potent photocatalytic degradation efficiency, Mater. Lett. 182 (2016) 305–308.
[28] H. Zeng, Y. Liu, Z. Xu, Y. Wang, Y. Chai, R. Yuan, H. Liu, Construction of a Z-scheme g-C_3N_4/Ag/AgI heterojunction for highly selective photoelectrochemical detection of hydrogen sulfide, Chem. Commun. 55 (2019) 11940–11943.
[29] Q. Zhang, J. Deng, Z. Xu, M. Chaker, D. Ma, High-efficiency broadband C_3N_4 photocatalysts: synergistic effects from upconversion and plasmons, ACS Catal. 7 (2017) 6225–6234.
[30] X. Sun, W. He, X. Hao, H. Ji, W. Liu, Z. Cai, Surface modification of BiOBr/TiO_2 by reduced AgBr for solar-driven PAHs degradation: mechanism insight and application assessment, J. Hazard. Mater. 412 (2021), 125221.
[31] J. Liu, N. Ma, W. Wu, Q. He, Recent progress on photocatalytic heterostructures with full solar spectral responses, Chem. Eng. J. 393 (2020), 124719.
[32] M. Zhu, M. Fujitsuka, L. Zeng, M. Liu, T. Majima, Dual function of graphene oxide for assisted exfoliation of black phosphorus and electron shuttle in promoting visible and near-infrared photocatalytic H_2 evolution, Appl. Catal. B Environ. 256 (2019), 117864.
[33] M. Xu, G. Yang, H. Bi, J. Xu, L. Feng, D. Yang, Q. Sun, S. Gai, F. He, Y. Dai, C. Zhong, P. Yang, Combination of CuS and g-C_3N_4 QDs on upconversion nanoparticles for targeted photothermal and photodynamic cancer therapy, Chem. Eng. J. 360 (2019) 866–878.
[34] L. Feng, F. He, B. Liu, G. Yang, S. Gai, P. Yang, C. Li, Y. Dai, R. Lv, J. Lin, g-C_3N_4 coated upconversion nanoparticles for 808 nm near-infrared light triggered phototherapy and multiple imaging, Chem. Mater. 28 (2016) 7935–7946.
[35] E. Cheng, S. Zhou, M. Li, Z. Li, Synthesis of g-C_3N_4-based $NaYF_4$:Yb,Tm@TiO_2 ternary composite with enhanced Vis/NIR-driven photocatalytic activities, Appl. Surf. Sci. 410 (2017) 383–392.
[36] S. Ullah, E.P. Ferreira-Neto, C. Hazra, R. Parveen, H.D. Rojas-Mantilla, M. L. Calegaro, Y.E. Serge-Correales, U.P. Rodrigues-Filho, S.J.L. Ribeiro, Broad spectrum photocatalytic system based on $BiVO_4$ and $NaYbF_4$:Tm^{3+} upconversion particles for environmental remediation under UV–vis–NIR illumination, Appl. Catal. B Environ. 243 (2019) 121–135.
[37] M. Li, Z. Zheng, Y. Zheng, C. Cui, C. Li, Z. Li, Controlled growth of metal-organic framework on upconversion nanocrystals for NIR-enhanced photocatalysis, ACS Appl. Mater. Interfaces 9 (2017) 2899–2905.
[38] H. Bi, Y. Dai, P. Yang, J. Xu, D. Yang, S. Gai, F. He, B. Liu, C. Zhong, G. An, J. Lin, Glutathione mediated size-tunable UCNPs-Pt(IV)-$ZnFe_2O_4$ nanocomposite for multiple bioimaging guided synergetic therapy, Small 14 (2018), e1703809.
[39] J. Zhang, Y. Huang, L. Jin, F. Rosei, F. Vetrone, J.P. Claverie, Efficient upconverting multiferroic core@shell photocatalysts: visible-to-near-infrared photon harvesting, ACS Appl. Mater. Interfaces 9 (2017) 8142–8150.
[40] J. Shen, G. Chen, T.Y. Ohulchanskyy, S.J. Kesseli, Tunable near infrared to ultraviolet upconversion luminescence enhancement in (α-$NaYF_4$: Yb, Tm)/CaF_2 Core/Shell nanoparticles for In situ real-time recorded biocompatible photoactivation, Small 19 (2013) 3213–3321.
[41] P.F. Lim, K.H. Leong, L.C. Sim, W.D. Oh, Y.H. Chin, P. Saravanan, C. Dai, Mechanism insight of dual synergistic effects of plasmonic Pd-$SrTiO_3$ for enhanced solar energy photocatalysis, Appl. Phys. A 7 (2020) 1–10.
[42] C.H. Hak, L.C. Sim, K.H. Leong, P.F. Lim, Y.H. Chin, P. Saravanan, M/g-C_3N_4 (M= Ag, Au, and Pd) composite: synthesis via sunlight photodeposition and application towards the degradation of bisphenol A, Environ. Sci. Pollut. Res. 25 (2018) 25401–25412.
[43] Y. Yang, X. Zhang, C. Niu, H. Feng, P. Qin, H. Guo, C. Liang, L. Zhang, H. Liu, L. Li, Dual-channel charges transfer strategy with synergistic effect of Z-scheme heterojunction and LSPR effect for enhanced quasi-full-spectrum photocatalytic bacterial inactivation: new insight into interfacial charge transfer and molecular oxygen activation, Appl. Catal. B Environ. 264 (2020), 118465.
[44] K.H. Leong, A.A. Aziz, L.C. Sim, P. Saravanan, M. Jang, D. Bahnemann, Mechanistic insights into plasmonic photocatalysts in utilizing visible light, Beilstein J. Nanotechnol. 1 (2018) 628–648.
[45] P.Q.T. Do, V.T. Huong, N.T.T. Phuong, T.H. Nguyen, H.K.T. Ta, H. Ju, T.B. Phan, V. Phung, K.T.L. Trinh, N.H.T. Tran, The highly sensitive determination of serotonin by using gold nanoparticles (Au NPs) with a localized surface plasmon resonance (LSPR) absorption wavelength in the visible region, RSC Adv. 51 (2020) 30858–30869.